

1 **Relative humidity modulates the physicochemical processing of secondary brown carbon**
2 **formation from nighttime oxidation of furan and pyrrole**

3
4 Kunpeng Chen,¹ Caitlin Hamilton,² Bradley Ries,¹ Michael Lum,¹ Raphael Mayorga,² Linhui Tian,
5 ¹ Roya Bahreini,¹ Haofei Zhang,² Ying-Hsuan Lin^{1*}
6

7 ¹Department of Environmental Sciences, University of California, Riverside, California 92521,
8 United States

9 ²Department of Chemistry, University of California, Riverside, California 92521, United States

10
11 * Email: ying-hsuan.lin@ucr.edu, Tel.: +1-951-827-3785

12
13
14
15
16
17
18
19
20

21 **Abstract**

22 Light-absorbing secondary organic aerosols (SOA), also known as secondary brown carbon (BrC),
23 are major components of wildfire smoke that can have a significant impact on the climate system;
24 however, how environmental factors such as relative humidity (RH) influence their formation is
25 not fully understood, especially for heterocyclic SOA precursors. We conducted chamber
26 experiments to investigate secondary BrC formation from the nighttime oxidation of furan and
27 pyrrole, two primary heterocyclic SOA precursors in wildfires, in the presence of pre-existing
28 particles at RH < 20% and ~50%. Our findings revealed that increasing RH significantly affected
29 the size distribution dynamics of both SOAs, with pyrrole SOA showing a stronger potential to
30 generate ultrafine particles via intensive nucleation processes. Higher RH led to increased mass
31 fractions of oxygenated compounds in both SOAs, suggesting enhanced gas-phase and/or
32 multiphase oxidation under humid conditions. Moreover, higher RH reduced the mass absorption
33 coefficients of both BrC, contrasting with those from homocyclic precursors, due to the formation
34 of non-absorbing high-molecular-weight oxygenated compounds and the decreasing mass
35 fractions of molecular chromophores. Overall, our findings demonstrate the unique RH
36 dependence of secondary BrC formation from heterocyclic precursors, which may critically
37 modulate the radiative effects of wildfire smoke on climate change.

38

39 **KEYWORDS**

40 furan and pyrrole, secondary organic aerosols, size distribution dynamics, oxygenated compounds,
41 molecular chromophores

42 **Synopsis**

43 Relative humidity modulates the size distribution dynamics, chemical composition, and optical
44 properties of secondary brown carbon derived from the nighttime oxidation of furans and pyrroles,
45 which may in turn influence their radiative effects on climate.

46

47 **Introduction**

48 Light-absorbing aerosols from wildfires can affect the climate system by directly heating
49 the atmosphere and indirectly altering the aerosol-boundary-layer-monsoon interactions.¹⁻³ Over
50 the last few decades, climate change has increased the intensity and frequency of wildfires,⁴⁻⁶
51 releasing a massive amount of volatile organic compounds (VOCs) and aerosols into the
52 atmosphere.⁷⁻⁹ However, the impact of unabated wildfire emissions is highly uncertain due to the
53 less-constrained radiative effects of wildfire smoke, which are influenced by the composition of
54 smoke aerosols. The major component of smoke aerosols is organics (>95%),^{10, 11} contributing to
55 ~45-86% of the total aerosol light absorption.¹² A large fraction of smoke organics (~30-56%)
56 accounts for secondary organic aerosols (SOA),¹³ in which the light-absorbing component is
57 known as secondary brown carbon (BrC). Thus, secondary BrC plays a critical role in moderating
58 the climate impacts of wildfire smoke.

59 The formation of secondary BrC can be sensitive to the smoke environments.^{14, 15} In
60 particular, relative humidity (RH) is a well-known environmental factor that may alter SOA
61 composition and secondary BrC light absorption. Extensive research has revealed that changes in
62 RH can influence SOA formation by altering the gas-phase chemistry, gas-to-particle partitioning
63 of oxidation products, phase states of aerosols, reactive uptake of radicals, and heterogeneous
64 reactions of aerosol-phase constituents.¹⁶⁻²⁷ Prior studies also reported that higher RH increased
65 the mass absorption coefficients (MAC) of secondary BrC derived from homocyclic aromatic
66 precursors.²⁸⁻³⁰ The increased MAC was associated with changes in molecular chromophores as
67 RH increased, which may alter the wavelength dependence of MAC profiles.³⁰ On the other hand,
68 higher RH decreased the MAC of secondary BrC derived from α -pinene,³¹ suggesting that the
69 effect of RH on MAC may differ depending on the type of VOCs. It is noted that a rise in RH may

70 result in increased liquid water content in wildfire aerosols, where water-soluble organics can
71 contribute to a large portion (e.g., ~45% at 405 nm) of BrC light absorption.³² Despite the extensive
72 investigations, the effect of RH on secondary BrC formation remains inconclusive.

73 Heterocyclic VOCs are the second largest sources of wildfire SOA precursors, and they
74 are more reactive compared to homocyclic VOCs (e.g., phenolics) due to their hetero atoms.^{33, 34}
75 Common heterocyclic VOCs released by wildfire include furans and pyrroles,³⁴⁻³⁷ which account
76 for ~30% of nitrate radical (NO₃) loss via nighttime chemistry in wildfire plumes.³⁸ Furans have
77 greater emission factors but may generate less-absorbing BrC from nighttime chemistry, whereas
78 pyrroles exhibit the opposite behavior.^{35, 36, 39, 40} Secondary BrC formation from the nighttime
79 chemistry of furans and pyrroles has been widely studied under RH conditions below 20%,^{14, 15, 39-}
80 ⁴¹ a typical level in dry wildfire smokes (e.g., the Williams Fire smoke⁴²) or dry fire areas (e.g.,
81 western United States^{43, 44} and Africa in dry seasons^{45, 46}). In addition, there have been frequent
82 observations of humid wildfire smoke worldwide, particularly those at RH ~50%, in the past two
83 decades due to climate change.⁴⁷⁻⁴⁹ A prior study of secondary BrC from indole, which contains a
84 pyrrole ring in its structure, highlighted that the effects of RH on the light absorption properties of
85 secondary BrC from heterocyclic VOCs were complicated and greatly unconstrained.⁵⁰ Hence,
86 there was still a significant lack of process-level understanding regarding the secondary BrC
87 formation from heterocyclic VOCs at various levels of RH.

88 In this study, chamber experiments were conducted to investigate the effects of RH on the
89 secondary BrC formation from the nighttime oxidation of furan and pyrrole, the backbone
90 compounds of furans and pyrroles. For comparison, RH was controlled at <20% and ~50% to
91 simulate dry and humid environments, respectively, while pre-existing particles were introduced
92 in both RH so that the chamber conditions would be closer to the ambient atmosphere. The effects

93 of RH on particulate size distribution dynamics, SOA composition, BrC light absorption properties,
94 and molecular chromophores were examined to better understand how RH-related
95 physicochemical processing modulates the secondary BrC formation from furan and pyrrole and
96 their implications in the atmosphere. These results will provide more accurate representations of
97 wildfire-associated secondary BrC and aid in assessing their climate impacts.

98

99 **Methods**

100 **Chamber Experiments.** All the experiments were carried out in a 10 m³ Teflon fluorinated
101 ethylene propylene (FEP) film chamber at room temperature (20–25 °C) under dark conditions.
102 The room temperature was much lower than the temperature of wildfires but comparable to the
103 temperature of ambient atmosphere,^{47, 49, 51} where furan and pyrrole released from wildfires were
104 observed in field studies.^{34, 37} Temperature and RH were monitored by a RH-USB sensor (Omega
105 Engineering, Inc.) attached to the chamber. A constant output atomizer (TSI 3076) was used to
106 produce pre-existing particles using a 10 mM ammonium sulfate ((NH₄)₂SO₄, Acros Organics,
107 99%, extra pure) solution. The pre-existing particles had a mass concentration and the central
108 diameter of ~50 µg m⁻³ and ~50 nm, respectively, to simulate the background particles in wildfire
109 smoke.^{52, 53} Given that higher RH can introduce liquid water or increase the amount of liquid water
110 content in wildfire aerosols,^{48, 54} we generated dry pre-existing particles at RH <20% and wet
111 aqueous pre-existing particles at RH ~50%. Because our humid condition was between the
112 efflorescence RH and deliquescence RH of ammonium sulfate,⁵⁵ dry seed particles were produced
113 by passing through a silica-gel filled diffusion dryer, whereas wet aqueous seed particles were
114 produced without the dryer.⁵⁶ Chamber experiments without pre-existing particles were also

115 performed at both RH levels. These experiments serve as a benchmark for detailed discussions on
116 the potential mechanisms involved in SOA formation.

117 This study used furan (TCI America, >99%) and pyrrole (TCI America, >99%) as model
118 compounds of heterocyclic VOCs. Each experiment involved only one VOC, in which ~200 ppbv
119 of furan or pyrrole was injected into the chamber using ~15 lpm of zero air. The concentration of
120 VOCs was determined based on previous studies to ensure appropriate SOA mass concentrations
121 for online and offline analyses.^{14, 15, 40, 41} After 20 minutes of mixing, a mixture of NO₂ and O₃
122 (molar concentration ratio ~3:2) was injected into the chamber, wherein N₂O₅ was generated and
123 then decomposed to NO₃ radicals. O₃ was generated by an O₃ generator (A2Z Ozone 3G LAB)
124 with pure oxygen (flow rate of 0.2 lpm), while NO₂ was directly injected from a NO₂ cylinder
125 (4789 ppm, Airgas) with a flow rate of 0.5 lpm. Similar to prior studies of SOA formation under
126 humid conditions,^{20, 21} the NO₂–O₃ ratio ensured that NO₃ primarily drove the oxidation of pyrrole
127 and furan in our chamber. The NO₂–O₃ mixture was first reacted in a glass vessel (total flow rate
128 of 0.7 lpm and residence time of 206 s) before the chamber injection. The concentration of N₂O₅
129 produced in the glassware was estimated by modeling the reactions between NO₂ and O₃, and the
130 initial concentration ratio of N₂O₅ to furan (or pyrrole) was approximately 2:1. While it was
131 possible that O₃ residue was also introduced into the chamber along with N₂O₅, the reaction rate
132 constants (*k*) at room temperature and atmospheric pressure for “furan/pyrrole + NO₃” (*k*_{furan+NO₃}
133 = 1.4 × 10⁻¹² cm³ molecule⁻¹ s⁻¹; *k*_{pyrrole+NO₃} = 4.9 × 10⁻¹¹ cm³ molecule⁻¹ s⁻¹) are ~6 orders of
134 magnitude higher than those of “furan/pyrrole + O₃” (*k*_{furan+O₃} = 2.4 × 10⁻¹⁸ cm³ molecule⁻¹ s⁻¹;
135 *k*_{pyrrole+O₃} = 1.6 × 10⁻¹⁷ cm³ molecule⁻¹ s⁻¹).⁵⁷⁻⁵⁹ Therefore, the oxidation of pyrrole and furan in our
136 chamber was mostly driven by NO₃-initiated oxidation.

137 The injection of the NO_2 – O_3 mixture marked the start of experiments. The duration of each
138 experiment was ~2.2 hours, during which the SOA mass concentration reached a plateau.
139 Following this plateau, the generated SOA samples were collected on polytetrafluoroethylene
140 membrane filters (PTFE, 46.2 mm, 2.0 μm , Tisch Scientific) for subsequent offline analysis. The
141 collection flowrate was 20 lpm, and the collection time was 1.5 hours; each filter collected the
142 aerosols from 1.8 m^3 of chamber air. The experimental procedure was similar to the those reported
143 in prior studies of high-RH chamber experiments.^{20, 21} It has been noted that the chamber wall loss
144 of particles may be potentially different at different RH. However, in this study, the first-order
145 size-dependent particulate wall loss rates were comparable at both RH levels (Figure S1).
146 Although vapor wall loss of oxidized products can be increased by higher RH, our data showed an
147 increased trend of mass fractions of oxygenated composition in particle phase (Figure S2). Such
148 evidence indicates that the chamber interference at higher RH did not significantly hinder the
149 formation of highly oxidized products in SOA.²⁰ Experiments of each environmental condition
150 were repeated for three times (n=3) to confirm the reproducibility of observed phenomena and
151 determine the uncertainties (standard deviations) of reported values.

152 **Particulate Size Distribution and Compositional Analysis.** The number concentration and size
153 distribution of SOA were measured throughout the duration of the experiments by a scanning
154 electrical mobility spectrometer (SEMS, Brechtel Manufacturing Inc.) in the diameter range of
155 10–800 nm with 140 bins. The bulk composition and the *in situ* molecular composition were
156 characterized by a mini-aerosol mass spectrometer coupled with a compact time-of-flight mass
157 spectrometer (mAMS, Aerodyne Research Inc.)⁶⁰ and an iodide-adduct time-of-flight chemical ion
158 mass spectrometer coupled with the filter inlet for gases and aerosols system (FIGAERO-ToF-
159 CIMS, Aerodyne Research Inc.),⁶¹ respectively. Attenuated total reflectance Fourier-transform

160 infrared spectrometer (ATR-FTIR, Thermo Nicolet iS50) was used to characterize the functional
161 group fingerprints. The measured IR spectra were deconvoluted using Igor Pro 7 (WaveMetrics,
162 Lake Oswego, OR, USA), in which the wavenumbers of identified peaks were determined. Gas
163 chromatography-electron ionization mass spectrometry (GC/EI-MS, Agilent Technologies 6890N
164 GC System and 5975 inert XL Mass Selective Detector) and liquid chromatography coupled with
165 an electrospray ionization source and a quadrupole-time-of-flight mass spectrometer (LC-ESI-Q-
166 ToFMS, Agilent Technologies 1260 Infinity II and 6545 Q-ToF LC/MS) were used to analyze the
167 molecular composition of SOA samples. Details of the instrumental setup have been published
168 elsewhere.^{40, 41} Particulate effective density, organic mass fraction in aerosols, and SOA mass
169 concentration in the chamber were calculated based on the methods described in our previous study
170 (Table S1).⁴⁰

171 The mass fractions of molecular chromophores were semi-quantified using surrogate
172 standards analyzed by LC-ESI-Q-TOFMS or GC/EI-MS. Molecular chromophores in furan BrC
173 were mainly carbonyls, while in pyrrole BrC accounted for both carbonyls and nitroaromatics.^{15,}
174 ⁴¹ Therefore, we used maleic acid (C₄H₄O₄), maleimide (C₄H₃NO₂), and nitropyrroles (C₄H₄N₂O₂,
175 including 2-nitropyrrole and 3-nitropyrrole) as surrogate standards for estimating chromophores in
176 furan BrC, carbonyl chromophores in pyrrole BrC, and nitroaromatic chromophores in pyrrole
177 BrC, respectively. C₄H₄O₄ was quantified by LC-ESI-Q-TOFMS, while C₄H₃NO₂ and C₄H₄N₂O₂
178 were quantified by GC/EI-MS with their authentic chemical standards. The mass fractions of other
179 molecular chromophores were estimated by eq 1.

$$180 \quad MF_{chromophore} = MF_{surrogate} \frac{c_{chromophore} M_{chromophore}}{c_{surrogate} M_{surrogate}} \\ 181 \quad = MF_{surrogate} R_F \frac{A_{chromophore} M_{chromophore}}{A_{surrogate} M_{surrogate}} \quad (1)$$

182 $MF_{chromophore}$ is the mass fraction of the characterized molecular chromophore in SOA
183 samples; $MF_{surrogate}$ is the mass fraction of the surrogate standard in SOA samples; $c_{chromophore}$ and
184 $c_{surrogate}$ are the molar concentrations of the characterized chromophores and the surrogate standard
185 in the SOA samples (mol L^{-1}); $M_{chromophore}$ and $M_{surrogate}$ are the molar masses of the characterized
186 chromophores and the surrogate standard in the SOA samples (g mol^{-1}); $A_{chromophore}$ and $A_{surrogate}$
187 are the peak areas of parent ions of the characterized chromophores and the surrogate standard in
188 their extracted ion chromatograms (EICs) measured by LC-ESI-Q-TOFMS. While the response
189 factor (R_F) of molecular chromophores may exhibit certain variations compared to surrogate
190 standards,¹⁵ semi-quantification can still offer approximate mass fractions to elucidate their
191 changes under different RH conditions.

192 **Light Absorption Properties.** The ultraviolet and visible (UV-vis) absorbance of SOA samples
193 was measured by a UV-vis spectrophotometer (Beckman DU-640) in the range of 290-700 nm,
194 with the reference wavelength at 700 nm. All of the SOA samples were extracted with acetonitrile
195 (ACN), an aprotic polar solvent that is suitable for analyzing carbonyl-rich secondary BrC
196 samples.⁴⁰ It should be noted that due to solvent selectivity, ACN may not completely extract the
197 furan SOA and pyrrole SOA constituents from filters (i.e., extraction efficiency < 100%).¹⁵ The
198 MAC profiles of SOA samples are calculated by eq 2.

199

$$MAC(\lambda) = \ln 10 \times \frac{A(\lambda) - A(700)}{b \times C_m} \quad (2)$$

200 $A(\lambda)$ is the wavelength (λ)-dependent absorbance, b is the light path length (i.e., 1 cm), and C_m
201 is the mass concentration of SOA. Since C_m was calculated by the total on-filter SOA mass (online-
202 monitored SOA mass concentration \times air volume in filter collection) over the volume of ACN
203 solution and given the chance that some BrC components were not completely extracted with ACN,
204 this study estimated the lower-bound limit of BrC MAC. Since SOA formation at each

205 environmental condition was repeated three times, the average and standard deviation of MAC at
 206 each wavelength can be calculated by three replicates of SOA samples. The relative error (i.e.,
 207 standard deviation over the average value) of the MAC value at each wavelength was ~15%, as
 208 estimated by 3 repeated experiments. The wavelength dependency of $MAC(\lambda)$ was also
 209 investigated by fitting the absorption Ångström exponent (AAE), as defined by eq 3.

$$210 \quad AAE = -\frac{\ln MAC(\lambda) - \ln MAC(\lambda_0)}{\ln \lambda - \ln \lambda_0} = -\frac{\ln [MAC(\lambda)/MAC(\lambda_0)]}{\ln(\lambda/\lambda_0)} \quad (3)$$

211 Here, λ_0 represents the reference wavelength. The fitted AAE would be equal to the slope
 212 of the linear regression of $\ln[MAC(\lambda)/MAC(\lambda_0)]$ versus $-\ln(\lambda/\lambda_0)$ with a zero intercept. Since our
 213 previous studies reported that AAE can be different in the UV (290–400 nm) and visible (400–600
 214 nm) ranges,^{14, 39–41} we set λ_0 as 400 nm for fitting the AAE. However, since the AAE shown in our
 215 data can largely vary along with λ , we also derive the wavelength-dependent AAE in eq 4.

$$216 \quad AAE(\lambda) = -\frac{d \ln MAC(\lambda)}{d \ln \lambda} = -\frac{\lambda}{MAC(\lambda)} \frac{d MAC(\lambda)}{d \lambda} \approx -\frac{\lambda}{MAC(\lambda)} \frac{MAC(\lambda+\Delta\lambda) - MAC(\lambda-\Delta\lambda)}{2 \Delta\lambda} \quad (4)$$

217 The stepwise wavelength ($\Delta\lambda$) was set as 3 nm. $AAE(\lambda)$ was sketched by a stepwise scan to
 218 portray a more detailed wavelength dependency of MAC, while the fitted AAE values reflected
 219 the overall trend. These two representations of AAE can complementarily highlight the distinction
 220 of MAC profiles at different RH.

221 **Computational Methods.** Time-dependent density functional theory was employed to estimate
 222 the theoretical UV–vis spectra of molecular chromophores. All the computations were conducted
 223 using the Gaussian 16 program (revision C. 01).⁶² Geometrical optimization and the computation
 224 of line-center wavelengths and oscillator strengths were performed by the B3LYP functional^{63, 64}
 225 with the 6-311++G(d,p) basis set,⁶⁵ as suggested in previous studies.^{14, 66, 67} The ACN environment
 226 was simulated by the integral equation formalism extension of the polarizable continuum model.⁶⁸
 227 The theoretical UV–Vis spectra were generated by the GaussView 6 program. The validation of

228 our theoretical calculations was previously discussed in detail with similar BrC chromophores.⁶⁷
229 Cartesian coordinates for all the molecular structures are summarized in Table S2.

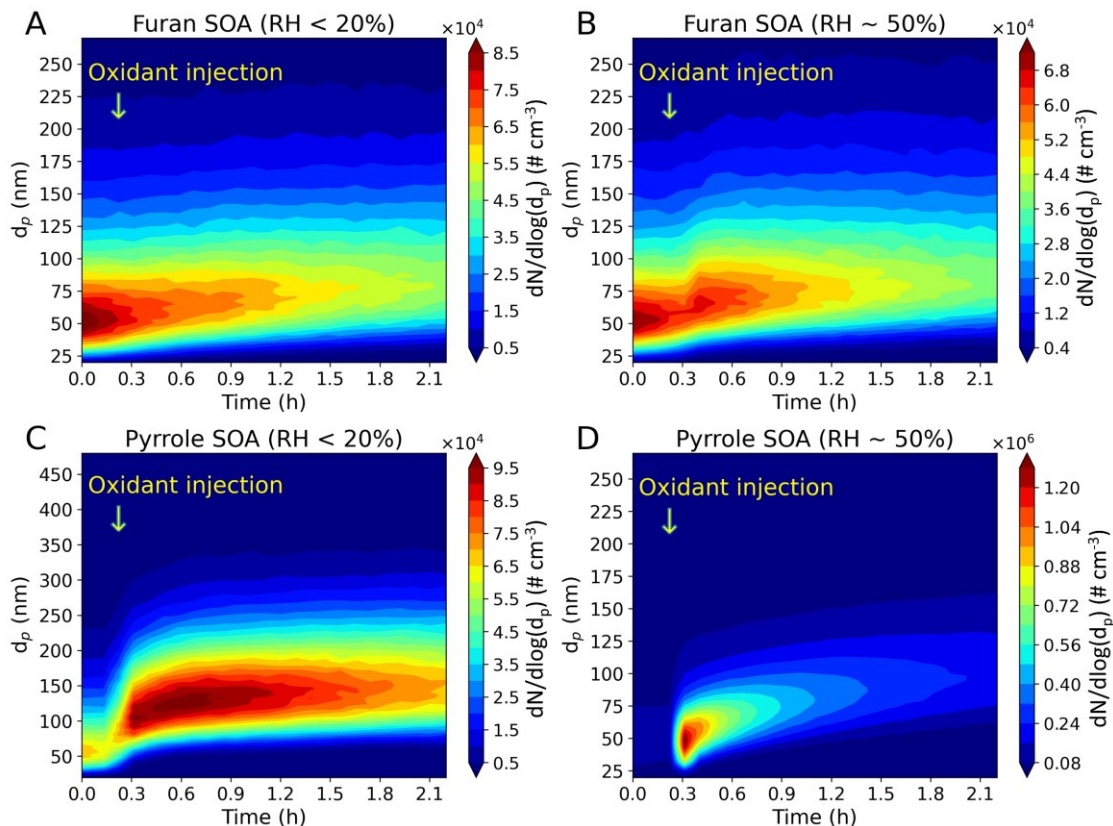
230

231 **Results and Discussions**

232 **Size Distribution Dynamics of Furan SOA and Pyrrole SOA.** Size distribution dynamics, which
233 encompasses the change in number and size distribution of particles over time, is the physical basis
234 of SOA formation and can be interconnected with gas-phase and/or multiphase chemistry.⁶⁹ At
235 RH <20%, the particulate size of furan SOA gradually increased over time, but at RH ~50%, the
236 particulate size of furan SOA rapidly increased within 10 minutes when furan oxidation started
237 (Figure 1 A, B). However, the particle size distribution dynamics of pyrrole SOA were different.
238 If the response of pyrrole SOA to changes in RH is similar to that of furan SOA, then an even
239 broader size distribution of pyrrole SOA should be observed at higher RH, because distinct growth
240 in particulate size was observed at low RH (Figure 1C), which indicated the greater potential of
241 pyrrole oxidation products to contribute to particles with larger size. However, at higher RH, our
242 results unexpectedly showed a much narrower size distribution of pyrrole SOA (Figure 1D). The
243 central diameter of the particles was still ~50 nm, comparable to that of the pre-existing particles,
244 reflecting the limited particulate growth. Correspondingly, the particle number concentration at
245 RH ~50% was significantly higher than that at RH <20% (Figure 1 C, D), indicating an intensive
246 new particle formation (NPF) at RH ~50%. The rapid decrease of number concentration in Figure
247 1D may be attributed to the chamber wall loss and coagulation of particles. Although the intensive
248 NPF was observed at a specific environmental condition (i.e., RH ~50% with pre-existing
249 particles), our findings can be tightly related to wildfire smoke because RH ~50% and pre-existing

250 particles are frequently observed in wildfire smoke.⁴⁷⁻⁴⁹ All of these characteristics demonstrated
251 the differential RH responses of furan SOA and pyrrole SOA.

252



253

254 **Figure 1.** Particle size distribution dynamics of (A) furan SOA at RH <20%; (B) furan SOA at RH
255 ~50%; (C) pyrrole SOA at RH <20%; (D) pyrrole SOA at RH ~50%.

256

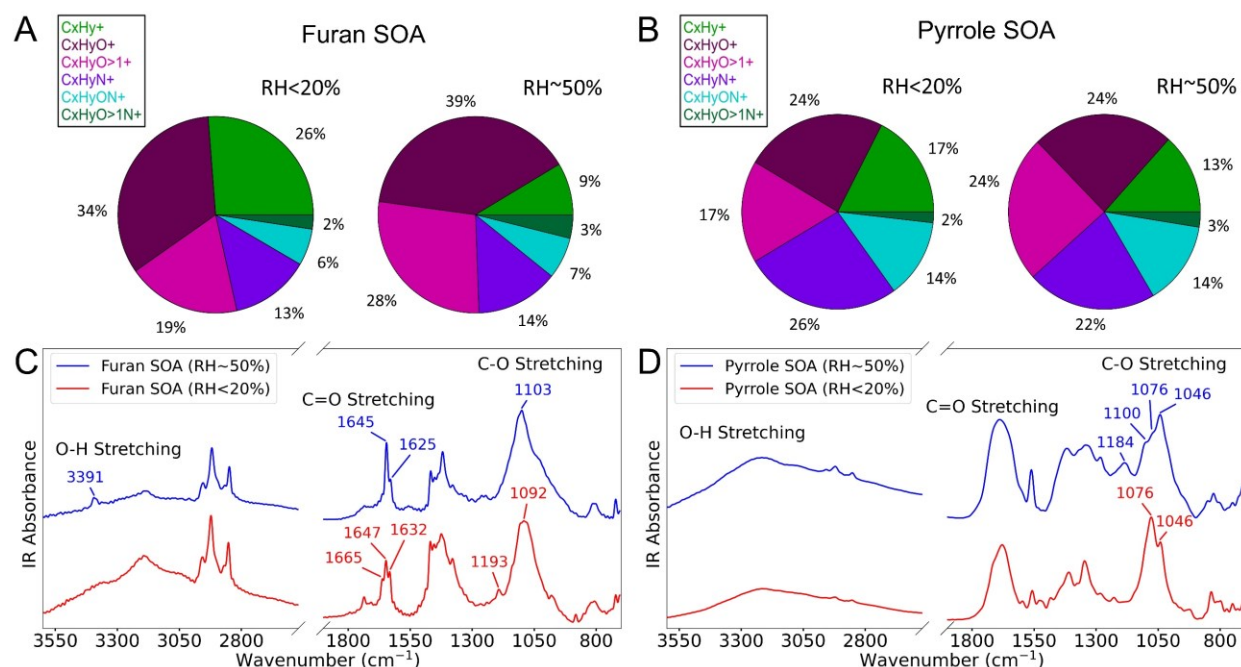
257 The intensive NPF of pyrrole SOA was unexpectedly associated with the pre-existing
258 particles, as revealed by our benchmark experiments. Without pre-existing particles, an increase
259 in RH broadened the size distribution of both SOAs when oxidation started (Figure S3). The size
260 distribution of pyrrole SOA at RH ~50% was much broader than that at RH <20% (Figure S3 C,
261 D), indicating that higher RH boosted particle growth accompanied by NPF so that the particulate
262 size was larger but the particulate number concentration was lower. This phenomenon reflected

263 that higher RH without pre-existing particles was capable of facilitating the condensation of gas-
264 phase products and the coagulation of ultrafine particles when pyrrole SOA was formed. These
265 two processes would be promoted in the presence of pre-existing particles, which were expected
266 to become the condensation sink.⁷⁰ However, intensive NPF was observed (Figure 1D), reflecting
267 the boosted nucleation process regardless of the pre-existing particles. It is noted that the potential
268 to form ultrafine particles via nucleation processes could be largely dependent on environmental
269 conditions. The intensive NPF shown in Figure 1D suggests that the nighttime oxidation of pyrrole
270 may have a stronger potential to induce nucleation in humid wildfire smoke. Although a thorough
271 mechanistic elucidation may require further measurements of the critical nuclei composition, the
272 unexpected NPF of pyrrole SOA can reflect that the nitrogen atom from the pyrrole backbone is
273 the key to inducing a stronger potential for nucleation, as compared to furan SOA (Figure 1 B, D).
274 The “furan-pyrrole” comparisons highlighted the importance of VOC-specified physicochemical
275 processing in wildfire-related SOA formation, which may influence the chemical composition.

276 **Chemical Characterization of SOA Composition.** To investigate the effects of RH on SOA
277 composition, chemical characterization was conducted using multiple complementary instruments
278 to determine the bulk and molecular compositions, as well as the molecular fingerprints. The bulk
279 composition of SOA showed that higher RH increased the mass fraction of $C_xH_yO_{>1}^+$ fragments
280 but decreased the mass fraction of $C_xH_y^+$ fragments in both SOAs (Figure 2 A, B). However, at
281 both RH conditions, the total mass fractions of nitrogen-containing fragments (i.e., $C_xH_yN^+$,
282 $C_xH_yON^+$, and $C_xH_yO_{>1}N^+$) of either furan SOA or pyrrole SOA were roughly consistent (Figure
283 2 A, B). It is noted that reduced nitrogen compounds (e.g., imidazole-type compounds) may be
284 potentially generated from particle-phase reactions between organic products and the ammonium
285 cations in the pre-existing particles.⁷¹⁻⁷⁵ Here, $C_2H_2N^+$, $C_2H_3N^+$, and $C_3H_3N^+$ (typical fragments of

286 nitrogen-containing organic compounds other than organonitrates measured by mAMS²⁹) were
 287 used to quantify the mass fractions of reduced nitrogen compounds (Table S3). At higher RH, the
 288 mass fraction of C₂H₃N⁺ was higher, but the mass fractions of C₂H₂N⁺ and C₃H₃N⁺ were lower.
 289 However, the total mass fraction of these fragments was roughly constant at both RH, indicating
 290 that the change in RH had a minor influence on the formation of reduced nitrogen. All these results
 291 indicated that the compositional change at higher RH mainly accounted for the generation of
 292 oxygenated products.

293



294 **Figure 2.** Chemical characterizations of the SOA bulk composition at RH <20% and ~50%
 295 conditions: (A) mass fractions of compositional fragments of furan SOA; (B) mass fractions of
 296 compositional fragments of pyrrole SOA; (C) functional group fingerprints of furan SOA; (D)
 297 functional group fingerprints of pyrrole SOA.

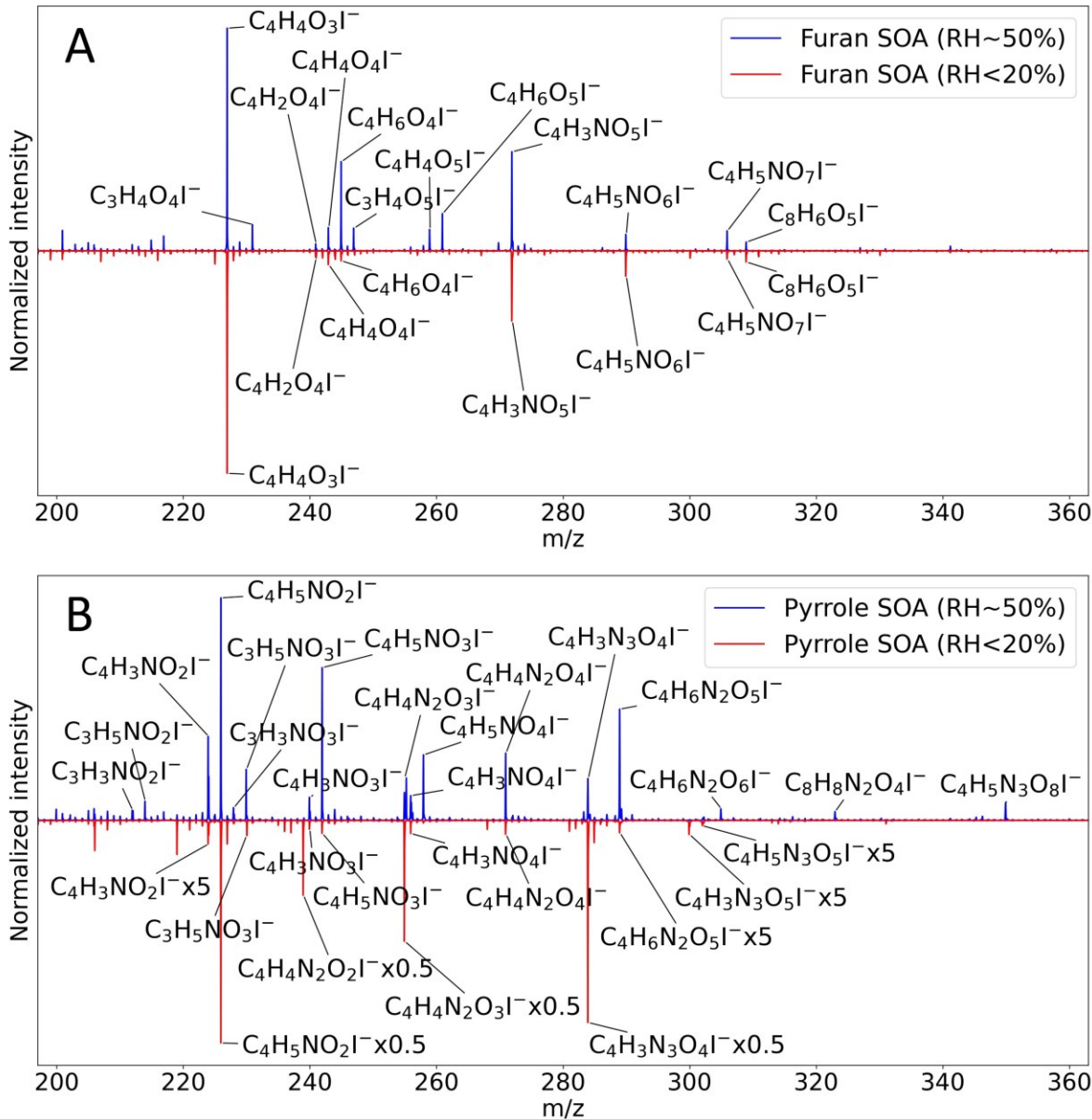
299

300 Moreover, our ATR-FTIR measurements showed the difference in oxygenated functional
301 group fingerprints at different RH, including the hydroxyl group (O–H) stretching, the
302 carbon–oxygen double bond (C=O) stretching, and the carbon–oxygen–carbon (C–O–C)
303 stretching (Figure 2). Functional groups were assigned to the wavenumbers based on previous IR
304 studies of SOA composition.⁷⁶ In furan SOA, the wavenumber of the C–O peak shifted while both
305 the number and wavenumbers of C=O peaks changed. A new O–H peak at 3391 cm^{−1} was observed,
306 but the C–O peak at 1193 cm^{−1} disappeared at higher RH (Figure 2C). These results indicated that
307 the change in RH may greatly alter the oxygenated constituents in furan SOA. While in pyrrole
308 SOA, O–H and C=O peaks were similar at both RH, while at higher RH two new C–O–C peaks
309 (1100 cm^{−1} and 1184 cm^{−1}) were identified (Figure 2D). Since the C–O–C structure cannot be
310 inherited from the pyrrole backbone, the new C–O–C peaks may be attributed to RH-modulated
311 gas-phase and/or multiphase oxidation on pyrrole SOA. The observed results of functional group
312 fingerprints from SOA formed at different RH levels reflected that higher RH could cause a shift
313 in the distribution of wavenumbers of oxygenated functional groups suggesting a considerable
314 change in the chemical composition of oxygenated compounds with RH.

315 The effect of RH on the oxygenated products was further investigated through the
316 molecular characterization of SOA samples. The average of the hydrogen-to-carbon (H/C) and the
317 oxygen-to-carbon (O/C) ratios (i.e., $\langle H/C \rangle$ and $\langle O/C \rangle$), weighted by intensity from FIGAERO-
318 ToF-CIMS measurements, of both SOA constituents increased with higher RH (Table S4). This
319 suggests that higher RH levels can enhance the saturation and oxygenation levels of SOA
320 constituents (Figure 3). The increasing $\langle H/C \rangle$ ratio decreased the intensity-weighted average of
321 double bond equivalence (DBE) (i.e., $\langle DBE \rangle$) (Figure 3). However, the nitrogen-to-carbon (N/C)
322 ratio (i.e., $\langle N/C \rangle$) decreased at higher RH in pyrrole SOA constituents while kept constant in furan

323 SOA constituents (Table S4), indicating that the formation of nitrogen-containing products in
324 pyrrole SOA characterized by FIGAERO-ToF-CIMS were more sensitive to RH change. In furan
325 SOA, the highest peaks at both RH conditions were attributed to $C_4H_4O_3$, while the presence of its
326 oxygenated products $C_4H_4O_4$ and $C_4H_4O_5$ was also observed (Figure 3A). It should be noted that
327 $C_4H_4O_5$ was only observed at higher RH, which may account for the enhanced oxygenation of
328 furan SOA constituents. In pyrrole SOA, the formation of new oxygenated products with higher
329 H/C and O/C ratios (e.g., $C_4H_6N_2O_6$, $C_4H_5N_3O_8$) was observed (Figure 3B). The peak intensity
330 ratios of $C_4H_5NO_3$ to $C_4H_5NO_2$ increased significantly at higher RH, contributing to the higher
331 oxygenation level of pyrrole SOA constituents at higher RH. All of these findings not only
332 confirmed the formation of oxygenated products at higher RH, but also demonstrated a higher
333 saturation level of SOA constituents. The increased saturation and oxygenation levels at higher
334 RH could be attributed to multiple processes, such as gas-phase chemistry, reactive uptake of
335 radicals, aerosol-phase reactions, etc.¹⁶⁻²⁷ Because multiple physicochemical processes interplay
336 during SOA formation, further research is necessary to provide a more comprehensive
337 understanding of the influence of each individual process involved. The compositional change due
338 to these processes may further affect the secondary BrC light absorption properties.

339



341 **Figure 3.** Molecular characterization of oxygenated products in (A) furan SOA and (B) pyrrole
342 SOA at RH <20% and ~50% conditions.

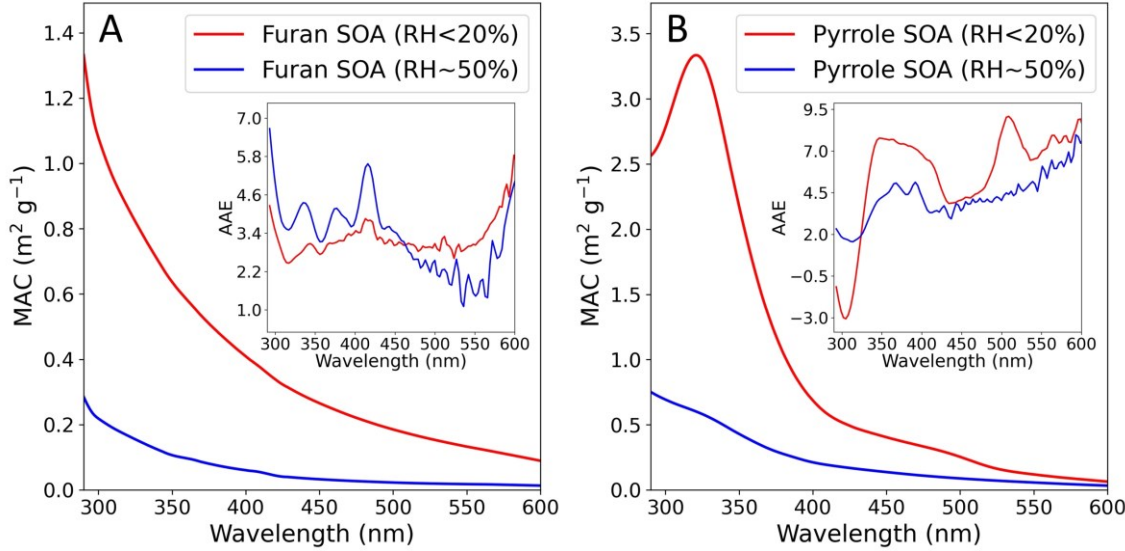
343

344 **Light Absorption Properties of Secondary BrC.** The light absorption properties of secondary
345 BrC can be affected by SOA compositional changes. Our results showed that higher RH
346 significantly reduced the MAC profiles for both SOAs, wherein both SOAs can fall in the

347 moderately absorptive BrC category at RH <20% and the weakly absorptive BrC category at RH
348 ~50% (Figure 4).⁷⁷ As compared with SOA derived from other precursors under various oxidation
349 conditions, furan SOA was moderately absorbing at RH <20% and least absorbing at RH ~50%,
350 while pyrrole SOA was highly absorbing at RH <20% and less absorbing at RH ~50% (Table
351 S5).^{28, 30, 50, 78} These comparisons indicated that the effects of RH on light absorption can be
352 sensitive to SOA precursors and their explicit chemical formation pathways.

353 The reduction in MAC profiles at higher RH cannot be attributed to the aqueous chemistry
354 between ammonium cations and SOA constituents,^{72, 79, 80} as these reactions may actually enhance
355 the MAC (Text S1; Figures S4 and S5). Instead, the reduced MAC observed at higher RH may be
356 linked to enhanced formation of oxygenated products. Our results showed that non-absorbing
357 oxygenated compounds (i.e., those with DBE = 0) were detected only at RH ~50% (Figure S6).
358 Some of the non-absorbing compounds were the major constituents in SOA samples (Figure S7).
359 These molecules have higher molecular weights and possess at least 8 carbons and 10 oxygens.
360 Such high level of oxygenation only observed at higher RH suggested that higher RH may reduce
361 MAC mostly via enhancing gas-phase and/or multiphase oxidation of SOA constituents.

362



363

364 **Figure 4.** MAC profiles of (A) furan BrC and (B) pyrrole BrC at both RH <20% and ~50%
365 conditions. The inset panels show the AAE changes along with wavelengths.

366

367 **Table 1.** Fitted AAE and R^2 in the linear regression of MAC in the UV (290–400 nm) and visible
368 (400–600 nm) ranges.

BrC Samples	RH	AAE		R^2	
		UV	Visible	UV	Visible
Furan BrC	<20%	3.00	3.21	1.00	1.00
	~50%	3.86	3.18	1.00	0.99
Pyrrole BrC	<20%	5.74	5.79	0.95	0.99
	~50%	3.88	4.07	0.99	1.00

369

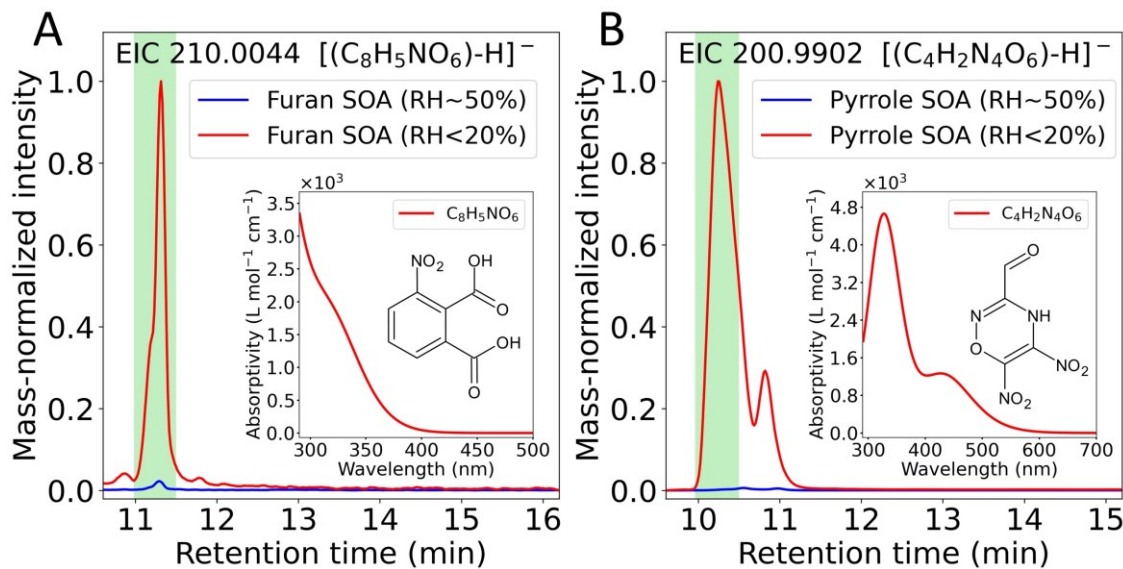
370 As illustrated by the AAE curves in the inset panels shown in Figure 4, the compositional
371 change of BrC chromophores was also reflected in the changed shape of MAC profiles. At both
372 RH conditions, the AAE curves of furan BrC were comparable, even though higher RH slightly

373 increased the AAE in the UV range but slightly decreased in the visible range (Figure 4A). The
374 fitted AAE showed comparable values at RH <20% and ~50% in both UV and visible ranges
375 (Table 1). However, the AAE curves of pyrrole BrC exhibited significant differences at RH <20%
376 and ~50%; a twisting curve was shown at RH <20%, whereas a monotonously increased trend with
377 a small bend was shown at RH ~50% (Figure 4B). The fitted AAE values were smaller at RH ~50%
378 (Table 1), indicating that the overall wavelength dependency of MAC profiles of pyrrole BrC was
379 diminished by higher RH levels. Taken together, the reduced MAC profiles with altered
380 wavelength dependency point to a change in the composition of BrC chromophores.

381 **Mass Fractions of BrC Chromophores in SOA.** The mass fractions of molecular chromophores
382 observed at both RH can aid in understanding the effect of RH on the MAC profiles. Semi-
383 quantification was performed for molecular chromophores characterized in this study (Table S6).
384 Most of the characterized chromophores listed in Table S6 were also reported in our previous
385 studies of furan- and pyrrole-derived secondary BrC.^{14, 15, 39-41} While the mass fractions of some
386 less abundant chromophores (e.g., C₄H₃NO₃) were similar at both RH, most of the characterized
387 chromophores showed lower mass fractions at higher RH. In Figure 5, two newly identified
388 compounds (C₈H₅NO₆ and C₄H₂N₄O₆) are presented as examples for detailed discussions.
389 C₈H₅NO₆ was characterized as 3-nitrophthalic acid (Figure S8A,C), whereas C₄H₂N₄O₆ showed
390 two peaks (Figure 5B), which corresponded to 5,6-dinitro-4H-1,2,4-oxadiazine-3-carbaldehyde
391 (Figure S8B,D) and 2,3,4-trinitro-pyrrole (Figure S9). At higher RH, the mass-normalized
392 intensity in their extracted ion chromatograms (EICs) nearly disappeared (Figure 5). Since
393 molecular chromophores have different contributions to the MAC profiles at different
394 wavelengths,¹⁵ their decreased mass fractions can reduce the MAC in specific wavelength regions.
395 Because the spectral absorption of 3-nitrophthalic acid only covers the UV range (Figure 5A), it

396 contributes to the reduction of MAC of furan BrC in the UV range. The reduction of MAC in the
 397 visible range may be attributed to the decreased mass fractions of other chromophores whose
 398 spectra can extend to above 400 nm (e.g., $C_4H_2O_4$).¹⁵ The spectral absorption of 5,6-dinitro-4H-
 399 1,2,4-oxadiazine-3-carbaldehyde covers both UV and visible ranges (Figure 5B), with a spectral
 400 shape similar to the MAC profile of pyrrole BrC at low RH (Figure 4B). More chromophores, such
 401 as 2,3,4-trinitro-pyrrole (Figure S9A) and dinitro-pyrroles ($C_4H_3N_3O_4$),⁴¹ can also contribute to the
 402 MAC profiles in the UV range. While it is possible that higher RH may potentially facilitate the
 403 production of new molecular chromophores with a red shift of light absorption towards longer
 404 wavelengths,³⁰ our findings revealed that the decrease in mass fractions of various molecular
 405 chromophores was mostly responsible for the altered wavelength dependency and lowered profiles
 406 of the MAC. The evidence together demonstrates the important role of molecular chromophores
 407 in bridging the change in environmental conditions to the light absorption properties of secondary
 408 BrC.

409



410

411 **Figure 5.** Characterization of molecular chromophores at RH <20% and ~50% conditions: (A)
412 C₈H₅NO₆ in furan SOA; (B) C₄H₂N₄O₆ in pyrrole SOA. The mass-normalized intensity was
413 calculated by the EIC intensity over the estimated mass of SOA samples, with the maximum value
414 in each panel scaled to 1.0. The inset panels show the theoretical UV–vis spectra of molecular
415 chromophores.

416

417 **Atmospheric Implications**

418 This study provides evidence for the role of RH in modulating secondary BrC formation
419 from heterocyclic VOCs, a significant group of SOA precursors in wildfire smoke,³⁴ through
420 changes in size distribution dynamics, chemical composition, and light absorption properties. We
421 also highlight the necessity of understanding explicit physicochemical pathways for evaluating the
422 effects of RH on the climate impacts of wildfire smoke aerosols because multiple physicochemical
423 processes can interplay during SOA formation, which can in turn alter the secondary BrC chemical
424 composition and light absorption properties. The observations presented in this study demonstrate
425 the intercorrelation of aerosol size distribution, chemical composition, and light absorption
426 properties. Specifically, the increased saturation and oxygenation levels of SOA composition at
427 higher RH may promote the formation of non-absorbing oxygenated compounds, which can lead
428 to decreased MAC profiles. Such process-level knowledge can aid in better understanding the
429 effects of RH on BrC light absorption in wildfire smoke.

430 In contrast to secondary BrC derived from homocyclic VOCs (e.g., toluene), in which the
431 production of nitroaromatic chromophores can be enhanced by higher RH,^{28, 81, 82} our findings
432 indicate that higher RH can lead to decreased mass fractions of nitrogen-containing chromophores
433 (e.g., C₈H₅NO₆ and C₄H₂N₄O₆) in furan- and pyrrole-derived BrC. Such a difference highlights

434 the critical role of SOA precursors and the molecular characteristics of chromophores in the effects
435 of RH on secondary BrC formation. It should be noted that RH may exhibit a more complicated
436 influence on secondary BrC light absorption (e.g., the non-monotonic RH dependency of MAC⁵⁰,
437 ⁸²) or have less significant effects if the nitrogen content of secondary BrC is limited.⁸² Given this
438 complexity, understanding the explicit physicochemical processes of SOA formation would be the
439 key to regulating secondary BrC formation. Our findings reveal that RH can greatly modulate the
440 explicit physicochemical processing of secondary BrC formation and further alter the BrC-related
441 radiative impacts of wildfire smoke. Therefore, this study highlights the importance of considering
442 RH as a critical environmental factor in more accurate assessments of the climate effects of
443 wildfire smoke aerosols.

444 Furthermore, this study can serve as a benchmark to help understand how the complex
445 atmospheric environment affects the climate impacts of smoke aerosols at the process level. Our
446 findings reveal that dry conditions can lead to strongly absorbing secondary BrC derived from the
447 nighttime oxidation of heterocyclic VOCs. This route may partially contribute to the strong BrC
448 light absorption in dry wildfire smoke, as evident from recent field studies.^{12, 83} More importantly,
449 the reduced light absorption and the enhanced oxygenated mass were not only found in the NO₃-
450 driven secondary BrC formation, but also in the aging processes of biomass-burning aerosols.^{84, 85}
451 This common characteristic suggests that the processing-level understanding reported in this study
452 may be partially applicable to a wider range of physicochemical processes related to wildfire
453 smoke. In addition, while previous studies have highlighted the importance of low-volatility high-
454 molecular-weight (≥ 400 Da) chromophores in optical properties of primary combustion BrC,^{77, 86-}
455 ⁸⁸ this study and our prior work of furan SOA and pyrrole SOA suggest that nighttime oxidation
456 of heterocyclic VOCs may mainly contribute to BrC chromophores with low molecular weight

457 (<400 Da) in wildfire smoke aerosols.^{14, 15, 39-41} Further research is needed to incorporate our
458 findings into climate models to better estimate the RH influence on the radiative effects of wildfire
459 smoke. Overall, our study demonstrates that environmental conditions such as RH in wildfire
460 smoke can modulate secondary BrC formation and hence regulate the radiative impacts of
461 unabated wildfires in the context of climate change.

462 **ASSOCIATED CONTENT**

463 **Supporting Information**

464 Details about the supplementary experiments; Cartesian coordinates for geometrical structures of
465 molecular chromophores in the TD-DFT calculations; summary of particulate effective density,
466 organic mass fraction, and mass concentration of generated SOA; mass fractions of the imidazole-
467 type fragments in SOA; intensity-weighted average and standard deviation of H/C, O/C, N/C ratios
468 and DBE of SOA composition characterized by FIGAERO-ToF-CIMS; MAC₃₆₅ from this study
469 and prior studies of secondary BrC; mass fractions of molecular chromophores in SOA; first-order
470 wall loss rate constants at both RH; Time series of C_xH_yO_{>1}⁺ and C_xH_y⁺; SOA size distribution
471 dynamics without pre-existing particles; MAC profiles in the solution experiments; characterized
472 products from aqueous-phase chemistry; extracted ion chromatograms of non-absorbing
473 oxygenated compounds; base peak chromatograms of SOA samples and selected non-absorbing
474 oxygenated compounds; characterization of 3-nitrophthalic acid and 5,6-dinitro-4H-1,2,4-
475 oxadiazine-3-carbaldehyde; characterization of 2,3,4-trinitro-pyrrole.

476

477 **AUTHOR INFORMATION**

478 **Corresponding Author**

479 * Email: ying-hsuan.lin@ucr.edu, Tel.: +1-951-827-3785

480 **Notes**

481 The authors declare no competing financial interest.

482

483 **ACKNOWLEDGEMENTS**

484 This work was supported by NSF AGS-1953905 and the UCR Hellman Fellowship granted to
485 Ying-Hsuan Lin. Michael Lum was supported by an NSF graduate research fellowship. We thank
486 Dr. Jie Zhou and Dr. Lingchao Zhu at UCR Analytical Chemistry Instrumentation Facility (ACIF)
487 for their assistance with UPLC-ESI-Q-TOFMS (supported by NSF CHE-0541848) and Thermo
488 Nicolet 6700 ATR-FTIR (supported by UCR Chemistry ACIF Fund).

489 **References**

490 1. Ferrero, L.; Močnik, G.; Cogliati, S.; Gregorič, A.; Colombo, R.; Bolzacchini, E., Heating
491 Rate of Light Absorbing Aerosols: Time-Resolved Measurements, the Role of Clouds, and Source
492 Identification. *Environ. Sci. Technol.* **2018**, *52*, (6), 3546-3555.

493 2. Liu, D.; He, C.; Schwarz, J. P.; Wang, X., Lifecycle of light-absorbing carbonaceous
494 aerosols in the atmosphere. *npj Clim. Atmos. Sci.* **2020**, *3*, (1), 40.

495 3. Ding, K.; Huang, X.; Ding, A.; Wang, M.; Su, H.; Kerminen, V.-M.; Petäjä, T.; Tan, Z.;
496 Wang, Z.; Zhou, D.; Sun, J.; Liao, H.; Wang, H.; Carslaw, K.; Wood, R.; Zuidema, P.; Rosenfeld,
497 D.; Kulmala, M.; Fu, C.; Pöschl, U.; Cheng, Y.; Andreae, M. O., Aerosol-boundary-layer-monsoon
498 interactions amplify semi-direct effect of biomass smoke on low cloud formation in Southeast Asia.
499 *Nat. Commun.* **2021**, *12*, (1), 6416.

500 4. Bowman, D. M. J. S.; Balch, J. K.; Artaxo, P.; Bond, W. J.; Carlson, J. M.; Cochrane, M.
501 A.; D'Antonio, C. M.; DeFries, R. S.; Doyle, J. C.; Harrison, S. P.; Johnston, F. H.; Keeley, J. E.;
502 Krawchuk, M. A.; Kull, C. A.; Marston, J. B.; Moritz, M. A.; Prentice, I. C.; Roos, C. I.; Scott, A.
503 C.; Swetnam, T. W.; van der Werf, G. R.; Pyne, S. J., Fire in the Earth System. *Science* **2009**, *324*,
504 (5926), 481-484.

505 5. Jolly, W. M.; Cochrane, M. A.; Freeborn, P. H.; Holden, Z. A.; Brown, T. J.; Williamson,
506 G. J.; Bowman, D. M. J. S., Climate-induced variations in global wildfire danger from 1979 to
507 2013. *Nat. Commun.* **2015**, *6*, (1), 7537.

508 6. Goss, M.; Swain, D. L.; Abatzoglou, J. T.; Sarhadi, A.; Kolden, C. A.; Williams, A. P.;
509 Diffenbaugh, N. S., Climate change is increasing the likelihood of extreme autumn wildfire
510 conditions across California. *Environ. Res. Lett.* **2020**, *15*, (9), 094016.

511 7. Andreae, M. O.; Merlet, P., Emission of trace gases and aerosols from biomass burning.

512 *Global Biogeochemical Cycles* **2001**, *15*, (4), 955-966.

513 8. Andreae, M. O., Emission of trace gases and aerosols from biomass burning – an updated

514 assessment. *Atmos. Chem. Phys.* **2019**, *19*, (13), 8523-8546.

515 9. Szopa, S., V. Naik, B. Adhikary, P. Artaxo, T. Berntsen, W.D. Collins, S. Fuzzi, L.

516 Gallardo, A. Kiendler-Scharr, Z. Klimont, H. Liao, N. Unger, P. Zanis, *Short-Lived Climate*

517 *Forcers. In Climate Change 2021: The Physical Science Basis. Contribution of Working Group I*

518 *to the Sixth Assessment Report of the Intergovernmental Panel on Climate Change [Masson-*

519 *Delmotte, V., P. Zhai, A. Pirani, S.L. Connors, C. Péan, S. Berger, N. Caud, Y. Chen, L. Goldfarb,*

520 *M.I. Gomis, M. Huang, K. Leitzell, E. Lonnoy, J.B.R. Matthews, T.K. Maycock, T. Waterfield, O.*

521 *Yelekçi, R. Yu, and B. Zhou (eds.)].* Cambridge University Press, Cambridge, United Kingdom and

522 New York, NY, USA: 2021; p 817–922.

523 10. Bond, T. C.; Streets, D. G.; Yarber, K. F.; Nelson, S. M.; Woo, J.-H.; Klimont, Z., A

524 technology-based global inventory of black and organic carbon emissions from combustion. *J.*

525 *Geophys. Res. Atmos.* **2004**, *109*, D14203.

526 11. Yu, P.; Toon, O. B.; Bardeen, C. G.; Zhu, Y.; Rosenlof, K. H.; Portmann, R. W.;

527 Thornberry, T. D.; Gao, R.-S.; Davis, S. M.; Wolf, E. T.; de Gouw, J.; Peterson, D. A.; Fromm,

528 M. D.; Robock, A., Black carbon lofts wildfire smoke high into the stratosphere to form a persistent

529 plume. *Science* **2019**, *365*, (6453), 587-590.

530 12. Chakrabarty, R. K.; Shetty, N. J.; Thind, A. S.; Beeler, P.; Sumlin, B. J.; Zhang, C.; Liu,

531 P.; Idrobo, J. C.; Adachi, K.; Wagner, N. L.; Schwarz, J. P.; Ahern, A.; Sedlacek, A. J.; Lambe,

532 A.; Daube, C.; Lyu, M.; Liu, C.; Herndon, S.; Onasch, T. B.; Mishra, R., Shortwave absorption by

533 wildfire smoke dominated by dark brown carbon. *Nat. Geosci.* **2023**, *16*, (8), 683-688.

534 13. Akherati, A.; He, Y.; Garofalo, L. A.; Hodshire, A. L.; Farmer, D. K.; Kreidenweis, S. M.;
535 Permar, W.; Hu, L.; Fischer, E. V.; Jen, C. N.; Goldstein, A. H.; Levin, E. J. T.; DeMott, P. J.;
536 Campos, T. L.; Flocke, F.; Reeves, J. M.; Toohey, D. W.; Pierce, J. R.; Jathar, S. H., Dilution and
537 photooxidation driven processes explain the evolution of organic aerosol in wildfire plumes.
538 *Environ. Sci. Atmos.* **2022**, 2, (5), 1000-1022.

539 14. Chen, K.; Mayorga, R.; Raeofy, N.; Lum, M.; Woods, M.; Bahreini, R.; Zhang, H.; Lin,
540 Y.-H., Effects of Nitrate Radical Levels and Pre-Existing Particles on Secondary Brown Carbon
541 Formation from Nighttime Oxidation of Furan. *ACS Earth Space Chem.* **2022**, 6, (11), 2709-2721.

542 15. Chen, K.; Mayorga, R.; Hamilton, C.; Bahreini, R.; Zhang, H.; Lin, Y.-H., Contribution of
543 Carbonyl Chromophores in Secondary Brown Carbon from Nighttime Oxidation of Unsaturated
544 Heterocyclic Volatile Organic Compounds. *Environ. Sci. Technol.* **2023**, 57, (48), 20085-20096.

545 16. Seinfeld, J. H.; Erdakos, G. B.; Asher, W. E.; Pankow, J. F., Modeling the Formation of
546 Secondary Organic Aerosol (SOA). 2. The Predicted Effects of Relative Humidity on Aerosol
547 Formation in the α -Pinene-, β -Pinene-, Sabinene-, $\Delta 3$ -Carene-, and Cyclohexene-Ozone Systems.
548 *Environ. Sci. Technol.* **2001**, 35, (9), 1806-1817.

549 17. Jonsson, Å. M.; Hallquist, M.; Ljungström, E., Impact of Humidity on the Ozone Initiated
550 Oxidation of Limonene, $\Delta 3$ -Carene, and α -Pinene. *Environ. Sci. Technol.* **2006**, 40, (1), 188-194.

551 18. Nguyen, T. B.; Roach, P. J.; Laskin, J.; Laskin, A.; Nizkorodov, S. A., Effect of humidity
552 on the composition of isoprene photooxidation secondary organic aerosol. *Atmos. Chem. Phys.*
553 **2011**, 11, (14), 6931-6944.

554 19. Saukko, E.; Lambe, A. T.; Massoli, P.; Koop, T.; Wright, J. P.; Croasdale, D. R.; Pedernera,
555 D. A.; Onasch, T. B.; Laaksonen, A.; Davidovits, P.; Worsnop, D. R.; Virtanen, A., Humidity-

556 dependent phase state of SOA particles from biogenic and anthropogenic precursors. *Atmos. Chem.*
557 *Phys.* **2012**, *12*, (16), 7517-7529.

558 20. Boyd, C. M.; Sanchez, J.; Xu, L.; Eugene, A. J.; Nah, T.; Tuet, W. Y.; Guzman, M. I.; Ng,
559 N. L., Secondary organic aerosol formation from the β -pinene+NO₃ system: effect of humidity
560 and peroxy radical fate. *Atmos. Chem. Phys.* **2015**, *15*, (13), 7497-7522.

561 21. Boyd, C. M.; Nah, T.; Xu, L.; Berkemeier, T.; Ng, N. L., Secondary Organic Aerosol (SOA)
562 from Nitrate Radical Oxidation of Monoterpenes: Effects of Temperature, Dilution, and Humidity
563 on Aerosol Formation, Mixing, and Evaporation. *Environ. Sci. Technol.* **2017**, *51*, (14), 7831-7841.

564 22. Stirnweis, L.; Marcolli, C.; Dommen, J.; Barmet, P.; Frege, C.; Platt, S. M.; Bruns, E. A.;
565 Krapf, M.; Slowik, J. G.; Wolf, R.; Prévôt, A. S. H.; Baltensperger, U.; El-Haddad, I., Assessing
566 the influence of NO_x concentrations and relative humidity on secondary organic aerosol yields
567 from α -pinene photo-oxidation through smog chamber experiments and modelling calculations.
568 *Atmos. Chem. Phys.* **2017**, *17*, (8), 5035-5061.

569 23. Liu, S.; Tsona, N. T.; Zhang, Q.; Jia, L.; Xu, Y.; Du, L., Influence of relative humidity on
570 cyclohexene SOA formation from OH photooxidation. *Chemosphere* **2019**, *231*, 478-486.

571 24. Petters, S. S.; Kreidenweis, S. M.; Grieshop, A. P.; Ziemann, P. J.; Petters, M. D.,
572 Temperature- and Humidity-Dependent Phase States of Secondary Organic Aerosols. *Geophys.*
573 *Res. Lett.* **2019**, *46*, (2), 1005-1013.

574 25. Chen, T.; Chu, B.; Ma, Q.; Zhang, P.; Liu, J.; He, H., Effect of relative humidity on SOA
575 formation from aromatic hydrocarbons: Implications from the evolution of gas- and particle-phase
576 species. *Sci. Total Environ.* **2021**, *773*, 145015.

577 26. Wang, Y.; Voliotis, A.; Shao, Y.; Zong, T.; Meng, X.; Du, M.; Hu, D.; Chen, Y.; Wu, Z.;
578 Alfarra, M. R.; McFiggans, G., Phase state of secondary organic aerosol in chamber photo-
579 oxidation of mixed precursors. *Atmos. Chem. Phys.* **2021**, *21*, (14), 11303-11316.

580 27. Liu, S.; Wang, Y.; Xu, X.; Wang, G., Effects of NO₂ and RH on secondary organic aerosol
581 formation and light absorption from OH oxidation of o-xylene. *Chemosphere* **2022**, *308*, 136541.

582 28. Liu, J.; Lin, P.; Laskin, A.; Laskin, J.; Kathmann, S. M.; Wise, M.; Caylor, R.; Imholt, F.;
583 Selimovic, V.; Shilling, J. E., Optical properties and aging of light-absorbing secondary organic
584 aerosol. *Atmos. Chem. Phys.* **2016**, *16*, (19), 12815-12827.

585 29. Cui, Y.; Frie, A. L.; Dingle, J. H.; Zimmerman, S.; Frausto-Vicencio, I.; Hopkins, F.;
586 Bahreini, R., Influence of Ammonia and Relative Humidity on the Formation and Composition of
587 Secondary Brown Carbon from Oxidation of 1-Methylnaphthalene and Longifolene. *ACS Earth
588 Space Chem.* **2021**, *5*, (4), 858-869.

589 30. Klodt, A. L.; Aiona, P. K.; MacMillan, A. C.; Ji Lee, H.; Zhang, X.; Helgestad, T.; Novak,
590 G. A.; Lin, P.; Laskin, J.; Laskin, A.; Bertram, T. H.; Cappa, C. D.; Nizkorodov, S. A., Effect of
591 relative humidity, NO_x, and ammonia on the physical properties of naphthalene secondary organic
592 aerosols. *Environ. Sci. Atmos.* **2023**, *3*, (6), 991-1007.

593 31. Song, C.; Gyawali, M.; Zaveri, R. A.; Shilling, J. E.; Arnott, W. P., Light absorption by
594 secondary organic aerosol from α -pinene: Effects of oxidants, seed aerosol acidity, and relative
595 humidity. *J. Geophys. Res. Atmos.* **2013**, *118*, (20), 11,741-11,749.

596 32. Sullivan, A. P.; Pokhrel, R. P.; Shen, Y.; Murphy, S. M.; Toohey, D. W.; Campos, T.;
597 Lindaas, J.; Fischer, E. V.; Collett Jr, J. L., Examination of brown carbon absorption from wildfires
598 in the western US during the WE-CAN study. *Atmos. Chem. Phys.* **2022**, *22*, (20), 13389-13406.

599 33. Gupta, R. R.; Kumar, M.; Gupta, V., Five-Membered Heterocycles with One Heteroatom.

600 In *Heterocyclic Chemistry: Volume II: Five-Membered Heterocycles*, Gupta, R. R.; Kumar, M.;

601 Gupta, V., Eds. Springer Berlin Heidelberg: Berlin, Heidelberg, 1999; pp 3-179.

602 34. Palm, B. B.; Peng, Q.; Fredrickson, C. D.; Lee, B. H.; Garofalo, L. A.; Pothier, M. A.;

603 Kreidenweis, S. M.; Farmer, D. K.; Pokhrel, R. P.; Shen, Y.; Murphy, S. M.; Permar, W.; Hu, L.;

604 Campos, T. L.; Hall, S. R.; Ullmann, K.; Zhang, X.; Flocke, F.; Fischer, E. V.; Thornton, J. A.,

605 Quantification of organic aerosol and brown carbon evolution in fresh wildfire plumes. *PNAS* **2020**,

606 *117*, (47), 29469.

607 35. Hatch, L. E.; Luo, W.; Pankow, J. F.; Yokelson, R. J.; Stockwell, C. E.; Barsanti, K. C.,

608 Identification and quantification of gaseous organic compounds emitted from biomass burning

609 using two-dimensional gas chromatography–time-of-flight mass spectrometry. *Atmos. Chem. Phys.*

610 **2015**, *15*, (4), 1865-1899.

611 36. Koss, A. R.; Sekimoto, K.; Gilman, J. B.; Selimovic, V.; Coggon, M. M.; Zarzana, K. J.;

612 Yuan, B.; Lerner, B. M.; Brown, S. S.; Jimenez, J. L.; Krechmer, J.; Roberts, J. M.; Warneke, C.;

613 Yokelson, R. J.; de Gouw, J., Non-methane organic gas emissions from biomass burning:

614 identification, quantification, and emission factors from PTR-ToF during the FIREX 2016

615 laboratory experiment. *Atmos. Chem. Phys.* **2018**, *18*, (5), 3299-3319.

616 37. Permar, W.; Wang, Q.; Selimovic, V.; Wielgasz, C.; Yokelson, R. J.; Hornbrook, R. S.;

617 Hills, A. J.; Apel, E. C.; Ku, I. T.; Zhou, Y.; Sive, B. C.; Sullivan, A. P.; Collett Jr, J. L.; Campos,

618 T. L.; Palm, B. B.; Peng, Q.; Thornton, J. A.; Garofalo, L. A.; Farmer, D. K.; Kreidenweis, S. M.;

619 Levin, E. J. T.; DeMott, P. J.; Flocke, F.; Fischer, E. V.; Hu, L., Emissions of Trace Organic Gases

620 From Western U.S. Wildfires Based on WE-CAN Aircraft Measurements. *J. Geophys. Res. Atmos.*

621 **2021**, *126*, (11), e2020JD033838.

622 38. Decker, Z. C. J.; Zarzana, K. J.; Coggon, M.; Min, K.-E.; Pollack, I.; Ryerson, T. B.;
623 Peischl, J.; Edwards, P.; Dubé, W. P.; Markovic, M. Z.; Roberts, J. M.; Veres, P. R.; Graus, M.;
624 Warneke, C.; de Gouw, J.; Hatch, L. E.; Barsanti, K. C.; Brown, S. S., Nighttime Chemical
625 Transformation in Biomass Burning Plumes: A Box Model Analysis Initialized with Aircraft
626 Observations. *Environ. Sci. Technol.* **2019**, *53*, (5), 2529-2538.

627 39. Jiang, H.; Frie, A. L.; Lavi, A.; Chen, J. Y.; Zhang, H.; Bahreini, R.; Lin, Y.-H., Brown
628 Carbon Formation from Nighttime Chemistry of Unsaturated Heterocyclic Volatile Organic
629 Compounds. *Environ. Sci. Technol. Lett.* **2019**, *6*, (3), 184-190.

630 40. Chen, K.; Raeofy, N.; Lum, M.; Mayorga, R.; Woods, M.; Bahreini, R.; Zhang, H.; Lin,
631 Y.-H., Solvent effects on chemical composition and optical properties of extracted secondary
632 brown carbon constituents. *Aerosol Sci. Tech.* **2022**, *56*, (10), 917-930.

633 41. Mayorga, R.; Chen, K.; Raeofy, N.; Woods, M.; Lum, M.; Zhao, Z.; Zhang, W.; Bahreini,
634 R.; Lin, Y.-H.; Zhang, H., Chemical Structure Regulates the Formation of Secondary Organic
635 Aerosol and Brown Carbon in Nitrate Radical Oxidation of Pyrroles and Methylpyrroles. *Environ.*
636 *Sci. Technol.* **2022**, *56*, (12), 7761-7770.

637 42. Akagi, S. K.; Craven, J. S.; Taylor, J. W.; McMeeking, G. R.; Yokelson, R. J.; Burling, I.
638 R.; Urbanski, S. P.; Wold, C. E.; Seinfeld, J. H.; Coe, H.; Alvarado, M. J.; Weise, D. R., Evolution
639 of trace gases and particles emitted by a chaparral fire in California. *Atmos. Chem. Phys.* **2012**, *12*,
640 (3), 1397-1421.

641 43. Westerling, A. L.; Gershunov, A.; Brown, T. J.; Cayan, D. R.; Dettinger, M. D., Climate
642 and Wildfire in the Western United States. *Bull. Amer. Meteor. Soc.* **2003**, *84*, (5), 595-604.

643 44. Holden Zachary, A.; Swanson, A.; Luce Charles, H.; Jolly, W. M.; Maneta, M.; Oyler Jared,
644 W.; Warren Dyer, A.; Parsons, R.; Affleck, D., Decreasing fire season precipitation increased
645 recent western US forest wildfire activity. *PNAS* **2018**, *115*, (36), E8349-E8357.

646 45. Jiang, Y.; Zhou, L.; Raghavendra, A., Observed changes in fire patterns and possible
647 drivers over Central Africa. *Environ. Res. Lett.* **2020**, *15*, (9), 0940b8.

648 46. Ramo, R.; Roteta, E.; Bistinas, I.; van Wees, D.; Bastarrika, A.; Chuvieco, E.; van der Werf
649 Guido, R., African burned area and fire carbon emissions are strongly impacted by small fires
650 undetected by coarse resolution satellite data. *PNAS* **2021**, *118*, (9), e2011160118.

651 47. Hobbs, P. V.; Sinha, P.; Yokelson, R. J.; Christian, T. J.; Blake, D. R.; Gao, S.; Kirchstetter,
652 T. W.; Novakov, T.; Pilewskie, P., Evolution of gases and particles from a savanna fire in South
653 Africa. *J. Geophys. Res. Atmos.* **2003**, *108*, No. D13, 8485.

654 48. Junghenn Noyes, K.; Kahn, R.; Sedlacek, A.; Kleinman, L.; Limbacher, J.; Li, Z., Wildfire
655 Smoke Particle Properties and Evolution, from Space-Based Multi-Angle Imaging. *Remote Sens.*
656 **2020**, *12*, (22), 3823.

657 49. Huang, X.; Ding, K.; Liu, J.; Wang, Z.; Tang, R.; Xue, L.; Wang, H.; Zhang, Q.; Tan, Z.-
658 M.; Fu, C.; Davis, S. J.; Andreae, M. O.; Ding, A., Smoke-weather interaction affects extreme
659 wildfires in diverse coastal regions. *Science* **2023**, *379*, (6631), 457-461.

660 50. Baboomian, V. J.; He, Q.; Montoya-Aguilera, J.; Ali, N.; Fleming, L. T.; Lin, P.; Laskin,
661 A.; Laskin, J.; Rudich, Y.; Nizkorodov, S. A., Light absorption and scattering properties of indole
662 secondary organic aerosol prepared under various oxidant and relative humidity conditions.
663 *Aerosol Sci. Tech.* **2023**, *57*, (6), 532-545.

664 51. Dennison, P. E.; Charoensiri, K.; Roberts, D. A.; Peterson, S. H.; Green, R. O., Wildfire
665 temperature and land cover modeling using hyperspectral data. *Remote Sens. Environ.* **2006**, *100*,
666 (2), 212-222.

667 52. Strand, T.; Larkin, N.; Rorig, M.; Krull, C.; Moore, M., PM2.5 measurements in wildfire
668 smoke plumes from fire seasons 2005–2008 in the Northwestern United States. *J. Aerosol Sci.*
669 **2011**, *42*, (3), 143-155.

670 53. Ding, Y.; Cruz, I.; Freedman, F.; Venkatram, A., Improving spatial resolution of PM2.5
671 measurements during wildfires. *Atmos. Pollut. Res.* **2021**, *12*, (5), 101047.

672 54. Junghenn Noyes, K. T.; Kahn, R. A.; Limbacher, J. A.; Li, Z., Canadian and Alaskan
673 wildfire smoke particle properties, their evolution, and controlling factors, from satellite
674 observations. *Atmos. Chem. Phys.* **2022**, *22*, (15), 10267-10290.

675 55. Bertram, A. K.; Martin, S. T.; Hanna, S. J.; Smith, M. L.; Bodsworth, A.; Chen, Q.; Kuwata,
676 M.; Liu, A.; You, Y.; Zorn, S. R., Predicting the relative humidities of liquid-liquid phase
677 separation, efflorescence, and deliquescence of mixed particles of ammonium sulfate, organic
678 material, and water using the organic-to-sulfate mass ratio of the particle and the oxygen-to-carbon
679 elemental ratio of the organic component. *Atmos. Chem. Phys.* **2011**, *11*, (21), 10995-11006.

680 56. Liu, T.; Huang, D. D.; Li, Z.; Liu, Q.; Chan, M.; Chan, C. K., Comparison of secondary
681 organic aerosol formation from toluene on initially wet and dry ammonium sulfate particles at
682 moderate relative humidity. *Atmos. Chem. Phys.* **2018**, *18*, (8), 5677-5689.

683 57. Atkinson, R.; Aschmann, S. M.; Carter, W. P. L., Kinetics of the reactions of O₃ and OH
684 radicals with furan and thiophene at 298 ± 2 K. *Int. J. Chem. Kinet.* **1983**, *15*, (1), 51-61.

685 58. Atkinson, R.; Aschmann, S. M.; Winer, A. M.; Carter, W. P. L., Rate constants for the gas
686 phase reactions of OH radicals and O₃ with pyrrole at 295 ± 1 K and atmospheric pressure. *Atmos.*
687 *Environ.* **1984**, *18*, (10), 2105-2107.

688 59. Atkinson, R.; Aschmann, S. M.; Winer, A. M.; Carter, W. P. L., Rate constants for the gas-
689 phase reactions of nitrate radicals with furan, thiophene, and pyrrole at 295 .+-. 1 K and
690 atmospheric pressure. *Environ. Sci. Technol.* **1985**, *19*, (1), 87-90.

691 60. Bahreini, R.; Keywood, M. D.; Ng, N. L.; Varutbangkul, V.; Gao, S.; Flagan, R. C.;
692 Seinfeld, J. H.; Worsnop, D. R.; Jimenez, J. L., Measurements of Secondary Organic Aerosol from
693 Oxidation of Cycloalkenes, Terpenes, and m-Xylene Using an Aerodyne Aerosol Mass
694 Spectrometer. *Environ. Sci. Technol.* **2005**, *39*, (15), 5674-5688.

695 61. Lopez-Hilfiker, F. D.; Mohr, C.; Ehn, M.; Rubach, F.; Kleist, E.; Wildt, J.; Mentel, T. F.;
696 Lutz, A.; Hallquist, M.; Worsnop, D.; Thornton, J. A., A novel method for online analysis of gas
697 and particle composition: description and evaluation of a Filter Inlet for Gases and AEROSols
698 (FIGAERO). *Atmos. Meas. Tech.* **2014**, *7*, (4), 983-1001.

699 62. Frisch, M. J.; Trucks, G. W.; Schlegel, H. B.; Scuseria, G. E.; Robb, M. A.; Cheeseman, J.
700 R.; Scalmani, G.; Barone, V.; Petersson, G. A.; Nakatsuji, H.; Li, X.; Caricato, M.; Marenich, A.
701 V.; Bloino, J.; Janesko, B. G.; Gomperts, R.; Mennucci, B.; Hratchian, H. P.; Ortiz, J. V.; Izmaylov,
702 A. F.; Sonnenberg, J. L.; Williams; Ding, F.; Lipparini, F.; Egidi, F.; Goings, J.; Peng, B.; Petrone,
703 A.; Henderson, T.; Ranasinghe, D.; Zakrzewski, V. G.; Gao, J.; Rega, N.; Zheng, G.; Liang, W.;
704 Hada, M.; Ehara, M.; Toyota, K.; Fukuda, R.; Hasegawa, J.; Ishida, M.; Nakajima, T.; Honda, Y.;
705 Kitao, O.; Nakai, H.; Vreven, T.; Throssell, K.; Montgomery Jr., J. A.; Peralta, J. E.; Ogliaro, F.;
706 Bearpark, M. J.; Heyd, J. J.; Brothers, E. N.; Kudin, K. N.; Staroverov, V. N.; Keith, T. A.;
707 Kobayashi, R.; Normand, J.; Raghavachari, K.; Rendell, A. P.; Burant, J. C.; Iyengar, S. S.; Tomasi,

708 J.; Cossi, M.; Millam, J. M.; Klene, M.; Adamo, C.; Cammi, R.; Ochterski, J. W.; Martin, R. L.;

709 Morokuma, K.; Farkas, O.; Foresman, J. B.; Fox, D. J. *Gaussian 16 Rev. C.01*, Wallingford, CT,

710 2016.

711 63. Becke, A. D., Density-functional exchange-energy approximation with correct asymptotic

712 behavior. *Physical Review A* **1988**, *38*, (6), 3098-3100.

713 64. Stephens, P. J.; Devlin, F. J.; Chabalowski, C. F.; Frisch, M. J., Ab Initio Calculation of

714 Vibrational Absorption and Circular Dichroism Spectra Using Density Functional Force Fields.

715 *The Journal of Physical Chemistry* **1994**, *98*, (45), 11623-11627.

716 65. Ditchfield, R.; Hehre, W. J.; Pople, J. A., Self-Consistent Molecular-Orbital Methods. IX.

717 An Extended Gaussian-Type Basis for Molecular-Orbital Studies of Organic Molecules. *J. Chem.*

718 *Phys.* **1971**, *54*, (2), 724-728.

719 66. Jacquemin, D.; Perpète, E. A.; Scuseria, G. E.; Ciofini, I.; Adamo, C., TD-DFT

720 Performance for the Visible Absorption Spectra of Organic Dyes: Conventional versus Long-

721 Range Hybrids. *J. Chem. Theory Comput.* **2008**, *4*, (1), 123-135.

722 67. Chen, J. Y.; Rodriguez, E.; Jiang, H.; Chen, K.; Frie, A.; Zhang, H.; Bahreini, R.; Lin, Y.-

723 H., Time-Dependent Density Functional Theory Investigation of the UV-Vis Spectra of

724 Organonitrogen Chromophores in Brown Carbon. *ACS Earth Space Chem.* **2020**, *4*, (2), 311-320.

725 68. Mennucci, B.; Cammi, R.; Tomasi, J., Excited states and solvatochromic shifts within a

726 nonequilibrium solvation approach: A new formulation of the integral equation formalism method

727 at the self-consistent field, configuration interaction, and multiconfiguration self-consistent field

728 level. *J. Chem. Phys.* **1998**, *109*, (7), 2798-2807.

729 69. Shiraiwa, M.; Yee, L. D.; Schilling, K. A.; Loza, C. L.; Craven, J. S.; Zuend, A.; Ziemann,
730 P. J.; Seinfeld, J. H., Size distribution dynamics reveal particle-phase chemistry in organic aerosol
731 formation. *PNAS* **2013**, *110*, (29), 11746-11750.

732 70. Hamed, A.; Korhonen, H.; Sihto, S.-L.; Joutsensaari, J.; Järvinen, H.; Petäjä, T.; Arnold,
733 F.; Nieminen, T.; Kulmala, M.; Smith, J. N.; Lehtinen, K. E. J.; Laaksonen, A., The role of relative
734 humidity in continental new particle formation. *J. Geophys. Res. Atmos.* **2011**, *116*, D03202.

735 71. Kampf, C. J.; Jakob, R.; Hoffmann, T., Identification and characterization of aging
736 products in the glyoxal/ammonium sulfate system - implications for light-absorbing material in
737 atmospheric aerosols. *Atmos. Chem. Phys.* **2012**, *12*, (14), 6323-6333.

738 72. Aiona, P. K.; Lee, H. J.; Leslie, R.; Lin, P.; Laskin, A.; Laskin, J.; Nizkorodov, S. A.,
739 Photochemistry of Products of the Aqueous Reaction of Methylglyoxal with Ammonium Sulfate.
740 *ACS Earth Space Chem.* **2017**, *1*, (8), 522-532.

741 73. Huang, M.; Zhang, J.; Cai, S.; Liao, Y.; Zhao, W.; Hu, C.; Gu, X.; Fang, L.; Zhang, W.,
742 Characterization of particulate products for aging of ethylbenzene secondary organic aerosol in
743 the presence of ammonium sulfate seed aerosol. *J. Environ. Sci.* **2017**, *47*, 219-229.

744 74. Grace, D. N.; Sharp, J. R.; Holappa, R. E.; Lugos, E. N.; Sebold, M. B.; Griffith, D. R.;
745 Hendrickson, H. P.; Galloway, M. M., Heterocyclic Product Formation in Aqueous Brown Carbon
746 Systems. *ACS Earth Space Chem.* **2019**, *3*, (11), 2472-2481.

747 75. Lian, X.; Zhang, G.; Yang, Y.; Lin, Q.; Fu, Y.; Jiang, F.; Peng, L.; Hu, X.; Chen, D.; Wang,
748 X.; Peng, P. a.; Sheng, G.; Bi, X., Evidence for the Formation of Imidazole from Carbonyls and
749 Reduced Nitrogen Species at the Individual Particle Level in the Ambient Atmosphere. *Environ.*
750 *Sci. Technol. Lett.* **2021**, *8*, (1), 9-15.

751 76. Cao, G.; Yan, Y.; Zou, X.; Zhu, R.; Ouyang, F., Applications of Infrared Spectroscopy in
752 Analysis of Organic Aerosols. *Spectr. Anal. Rev.* **2018**, *06*, 12-32.

753 77. Saleh, R., From Measurements to Models: Toward Accurate Representation of Brown
754 Carbon in Climate Calculations. *Curr. Pollut. Rep.* **2020**, *6*, (2), 90-104.

755 78. Joo, T.; Machesky, J. E.; Zeng, L.; Hass-Mitchell, T.; Weber, R. J.; Gentner, D. R.; Ng, N.
756 L., Secondary Brown Carbon Formation From Photooxidation of Furans From Biomass Burning.
757 *Geophys. Res. Lett.* **2024**, *51*, (1), e2023GL104900.

758 79. Nguyen, T. B.; Lee, P. B.; Updyke, K. M.; Bones, D. L.; Laskin, J.; Laskin, A.; Nizkorodov,
759 S. A., Formation of nitrogen- and sulfur-containing light-absorbing compounds accelerated by
760 evaporation of water from secondary organic aerosols. *J. Geophys. Res. Atmos.* **2012**, *117*, D01207.

761 80. Nguyen, T. B.; Laskin, A.; Laskin, J.; Nizkorodov, S. A., Brown carbon formation from
762 ketoaldehydes of biogenic monoterpenes. *Faraday Discuss.* **2013**, *165*, (0), 473-494.

763 81. Lin, P.; Liu, J.; Shilling, J. E.; Kathmann, S. M.; Laskin, J.; Laskin, A., Molecular
764 characterization of brown carbon (BrC) chromophores in secondary organic aerosol generated
765 from photo-oxidation of toluene. *Phys. Chem. Chem. Phys.* **2015**, *17*, (36), 23312-23325.

766 82. Mitra, K.; Mishra, H. R.; Pei, X.; Pathak, R. K., Secondary Organic Aerosol (SOA) from
767 Photo-Oxidation of Toluene: 1 Influence of Reactive Nitrogen, Acidity and Water Vapours on
768 Optical Properties. *Atmosphere* **2022**, *13*, (7), 1099.

769 83. Cho, C.; Kim, S.-W.; Choi, W.; Kim, M.-H., Significant light absorption of brown carbon
770 during the 2020 California wildfires. *Sci. Total Environ.* **2022**, *813*, 152453.

771 84. Kodros, J. K.; Papanastasiou, D. K.; Paglione, M.; Masiol, M.; Squizzato, S.; Florou, K.;
772 Skyllakou, K.; Kaltsonoudis, C.; Nenes, A.; Pandis, S. N., Rapid dark aging of biomass burning
773 as an overlooked source of oxidized organic aerosol. *PNAS* **2020**, *117*, (52), 33028.

774 85. Schnitzler, E. G.; Gerrebos, N. G. A.; Carter, T. S.; Huang, Y.; Heald, C. L.; Bertram, A.
775 K.; Abbatt, J. P. D., Rate of atmospheric brown carbon whitening governed by environmental
776 conditions. *PNAS* **2022**, *119*, (38), e2205610119.

777 86. Wong, J. P. S.; Nenes, A.; Weber, R. J., Changes in Light Absorptivity of Molecular
778 Weight Separated Brown Carbon Due to Photolytic Aging. *Environ. Sci. Technol.* **2017**, *51*, (15),
779 8414-8421.

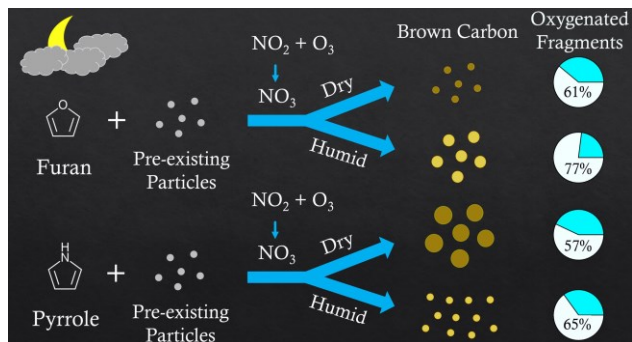
780 87. Wong, J. P. S.; Tsagkaraki, M.; Tsiodra, I.; Mihalopoulos, N.; Violaki, K.; Kanakidou, M.;
781 Sciare, J.; Nenes, A.; Weber, R. J., Atmospheric evolution of molecular-weight-separated brown
782 carbon from biomass burning. *Atmos. Chem. Phys.* **2019**, *19*, (11), 7319-7334.

783 88. Shetty, N.; Liu, P.; Liang, Y.; Sumlin, B.; Daube, C.; Herndon, S.; Goldstein, A. H.;
784 Chakrabarty, R. K., Brown carbon absorptivity in fresh wildfire smoke: associations with volatility
785 and chemical compound groups. *Environ. Sci. Atmos.* **2023**, *3*, (9), 1262-1271.

786

787

788 TOC Graphic



789